DIQ-MPM: Dual Interface Quadrature MPM for Simulating Large Deformation and Fluid-Solid Coupling

Kangrui Zhang, Ruihong Cen, Siyan Zhu, Ruoyan Chen and Bo Ren

Abstract—We present DIQ-MPM, a novel monolithic two-way coupling framework for simulating interactions between solids modeled with the total Lagrangian formulation and Eulerian incompressible fluids using the Material Point Method (MPM). Our approach combines an implicit TLMPM formulation with a mixed velocity-pressure scheme to robustly simulate compressible solids undergoing large deformations, while eliminating numerical fractures. To enable strong fluid–solid coupling without relying on overlapping grids, we introduce a Dual Interface Quadrature (DIQ) mechanism that maps fluid-solid interface information consistently between the current and reference configurations. This allows us to construct a unified sparse pressure-only system via Schur complement, leading to efficient and stable coupling. We also integrate a particle-based contact force model to resolve solid-solid and solid-boundary contacts within implicit TLMPM. Experimental results demonstrate that our method stably captures free-slip coupling, large deformation phenomena, and complex interactions between compressible solids and incompressible fluids.

Index Terms—physically based animation, hybrid method, material point method

1 Introduction

The coupling of multiple materials is widely present in natural phenomena and visual animations, constituting one of the core issues in physics-based simulation. Fluid simulation usually relies on Eulerian grids, while solid simulation tends to use Lagrangian particles. As a hybrid method that combines the advantages of grids and particles, Material Point Method(MPM) has received widespread attention in fluid-solid coupling problems. Interface Quadrature Material Point Method (IQ-MPM) [1] introduces a fully MPM-based fluid-solid coupling framework, incorporating a pressure variable into MPM solids to construct a monolithic pressure-only linear system. This formulation ensures stability and strictly enforces free-slip boundary conditions in two-way coupling between fluids and solids. IQ-MPM achieves high computational efficiency by solving a single symmetric positive definite (SPD) system per time step.

Conventional Eulerian MPM(EMPM) has the so-called cell-crossing issue [2] in solid simulations. Since its shape functions are linear, when a material point crosses Eulerian grids, the force on the grid (related to the derivative of the shape function) will become discontinuous and reduce the convergence rate. Moreover, when a solid body undergoes large deformation, the support of particles over the Eulerian grid may become insufficient and eventually lead to numerical stress concentration and fracture. Some improvements have been used to solve the cell-crossing issue, including quadratic/cubic B-spline interpolation [3] and generalized interpolation MPM(GIMP) [4]. In the graphics community, high-order B-spline interpolation is often used. However, unwanted numerical fractures still plague simulations and limit the potential impact of existing models. Recently, total Lagrangian MPM (TLMPM) [5] addressed these problems by fixing the reference configuration to the initial time step. TLMPM always calculates stress and time integration with respect to the initial grid, thereby ensuring that cell-crossing and numerical fracture will not occur in solid simulations.

On the other hand, EMPM adopts the current configuration as the reference, which is essential for simulating materials that experience frequent topological changes, such as fluids. Therefore, a simulation framework capable of handling both large deformation solids and fluid-solid coupling needs to integrate the advantages of TLMPM and EMPM. In computer graphics, Su et al. [6] proposed Arbitrary Updated Lagrangian MPM(A-ULMPM), which automatically handles solids and fluids in a unified framework by adaptively updating the reference configuration. A-ULMPM effectively prevents numerical fracture in solids and supports fluid simulations. However, it still uses the build-in contact mechanism of MPM for coupling simulation, leading to common sticky boundary artifacts in MPM-based fluid-solid coupling. A-ULMPM also does not consider the collisions between solids.

In this paper, we introduce a new MPM-based monolithic coupling framework for simulating interactions between total Lagrangian compressible solids and Eulerian incompressible fluids. We first formulate an implicit TLMPM with a penalty-based contact model, which enables stable simulation of large-deformation hyperelastic solids. To support coupling with incompressible flow, we extend TLMPM with a mixed velocity–pressure formulation derived from the variational weak form. In the coupling stage, we propose a novel dual interface quadrature method that uses the solid deformation map to consistently transfer interfacial

Kangrui Zhang, Ruoyan Chen and Bo Ren are with VCIP, College of Computer Science, Nankai University, Tianjin 300350, China.
Ruihong Cen is with School of Computing, National University of Singapore, 117417, Singapore
Siyan Zhu is with School of Computer Science and Engineering, Beihang University, Beijing 100191, China
Corresponding author: Bo Ren (rb@nankai.edu.cn).

0000–0000/00$00.00 © 2021 IEEE

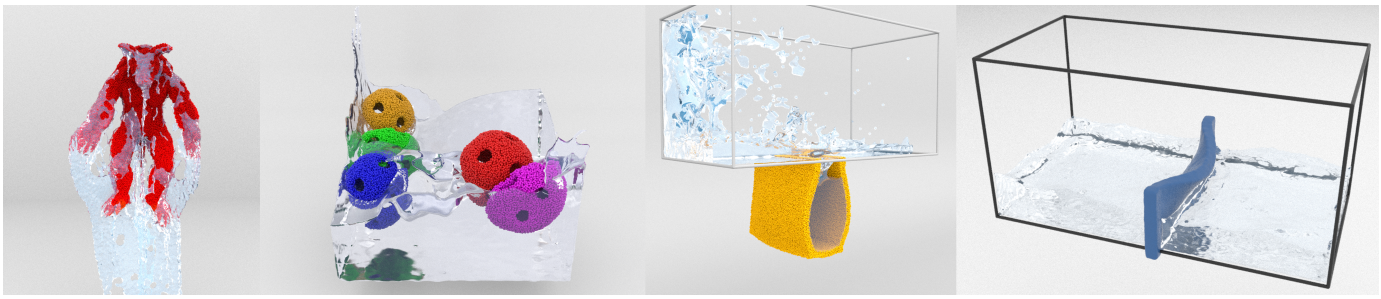

Fig. 1: Fluid-solid coupling simulations using DIQ-MPM. From left to right: water is poured onto a soft armadillo toy fixed in mid-air; toy balls of different densities drop into the water; After the dam breaks, the fluid falls into an elastic bag; the fluid impacts and flows over an elastic wall. Our new coupling framework simultaneously simulates fluid-solid coupling and large deformations of elastic bodies, while enforcing the free-slip boundary condition

quantities between the initial and current configurations. This formulation leads to a unified linear system that is finally reduced to a sparse, pressure-only system via Schur complement. To the best of our knowledge, this is the first MPM-based solver capable of handling strong two-way coupling between incompressible fluids and compressible solids undergoing large nonlinear deformation, without introducing numerical fracture artifacts. We also extend this mixed pressure and coupling mechanism to A-ULMPM for coupling solids with more general reference configurations, such as granular-like materials.

The contributions of this paper are:

- A monolithic MPM-based solver for strong two-way fluid-solid coupling without numerical fracture;
- A mixed velocity–pressure formulation for TLMPM and A-ULMPM that enables unified coupling with incompressible flow;
- A dual interface quadrature mechanism that stably and consistently couples Eulerian fluids with solids defined in different reference configurations.

2 Related Works

2.1 Fluid-Solid Coupling

Fluid-solid coupling has been widely studied in graphics. Cut-cell methods, designed for Lagrangian solid and Eulerian/Hybrid fluid coupling, clip the solid mesh against the background grid to improve interfacial boundary conditions. Roble et al. [7] first introduced cut-cell methods in graphics, modifying the pressure projection in fluid simulations. Batty et al. [8] used partial cell volume in the fluid dual-cell to derive a variational form of fluid-rigid coupling. Ng et al. [9] improved accuracy near boundaries using face ratio instead of volume ratio. Zarifi et al. [10] presented a monolithic SPD formulation for strong two-way fluid-elastic solid coupling. Takahashi et al. [11] applied the cut-cell method for fluid-solid and solid-solid coupling as an energy minimization problem. Cut-cell method could also be combined with Lattice-Boltzmann method for fluid-solid coupling [12]. Eulerian solid simulations [13]–[15] represent elastic bodies directly on an Eulerian grid; in particular, the coupling formulation of Teng et al. [15] advances a single velocity field shared by both solid and fluid during pressure projection, implicitly enforcing a no-slip boundary condition at the fluid-solid interface. Robinson-Mosher et al. [16] couple FEM solids to an Eulerian fluid grid by lumping fluid mass and momentum onto nearby solid nodes and solving a monolithic, momentum-conserving system. A key distinction is that our coupling formulation is fully particle-based, and therefore better suited to handling large deformations and topological changes, whereas FEM-based solids typically require additional techniques such as remeshing to maintain a mesh conforming to the solid.

Another prominent class of fluid–solid coupling methods uses mesh-free Lagrangian particles, notably Smoothed Particle Hydrodynamics (SPH) [17]. SPH methods inherently preserve mass and handle topological changes, making them suitable for complex fluid–solid interactions. Early SPH approaches modeled weakly compressible fluids via an equation of state (EOS) [18]. Later work extended SPH to simulate incompressible flows by solving the pressure Poisson equation directly on the particle distribution [19]. Bender et al. [20] improved the stability of incompressible SPH simulations by addressing both divergence and density errors. Akinci et al. [21] simulated SPH-rigid body coupling using boundary particles. Peer et al. [22] incorporated elastic solids into SPH with operator splitting for fluid–elastic coupling. Xie et al. [23] proposed a two-way coupling formulation for SPH fluids and FEM solids using interior point method. Kee et al. [24] enhanced SPH by optimizing time integration for large time steps. However, SPH-based fluid–solid coupling still faces stability issues, particularly in solid simulation, often requiring additional gradient correction [25]. Additionally, since SPH solids are embedded in an incompressible fluid framework, their use is mainly limited to incompressible scenarios.

2.2 Material Point Method

MPM was originally developed by Sulsky et al. [26], building upon the FLIP method [27], [28]. As a hybrid approach, MPM combines the strengths of Eulerian grids and Lagrangian particles, offering advantages in simulating large deformations and complex material behavior. Since its introduction into graphics, MPM has been widely adopted for a variety of materials, including snow [3], sand [29], and fluid–sediment interactions [30]. To mitigate pressure oscillations arising from soft constraints in weakly compressible MPM, Stomakhin et al. [31] proposed an augmented formulation that explicitly incorporates pressure into fluid

simulation. Zhang et al. [32] further improved incompressible MPM by discretizing velocity and pressure on a semi-staggered grid, which integrates more naturally into the MPM framework compared to MAC grids and reduces computational cost. Gagniere et al. [33] extended this idea by noting that continuous derivatives via B-spline interpolation are more conveniently obtained on semi-staggered layouts.

An important challenge in MPM simulation is how to enforce velocity discontinuities on the grid, especially in scenarios involving contact, fracture, or fluid-solid coupling. By default, MPM only supports no-slip contact behavior through automatic collision handling. Regarding contact modeling, Razon et al. [34] addressed numerical cohesion and momentum conservation in hybrid method, whereas Li et al. [35] guaranteed interpenetration-free MPM-FEM coupling. Jiang et al. [36] introduced an anisotropic elastoplastic model for frictional interactions. A more comprehensive solution involves assigning a separate grid to each contact object, performing independent MPM simulations on each grid, and resolving grid interactions explicitly. Yan et al. [37] and Fei et al. [38] employed this strategy to simulate multiphase fluid interactions and fluid–fabric coupling. To achieve more flexible boundary conditions, IQ-MPM [1] utilizes interface quadrature (IQ) points to monolithically couple solid and fluid velocity grids, enabling the enforcement of free-slip boundaries. Additional approaches have been proposed to handle velocity discontinuities in material separation and fracture. These typically involve dual-grid frameworks in which particles are dynamically assigned to one of the grids based on certain criteria. For example, Hu et al. [39] proposed a CPIC scheme for MPM-rigid body coupling in material cutting simulations. In fracture scenarios, phase-field gradients have been used to determine particle-grid assignments and enforce velocity discontinuity at material fracture interfaces [40], [41].

When simulating elastic materials, EMPM suffers from the cell-crossing instability and numerical fractures. Variants such as GIMP [42] and CPDI [43] have been developed but cannot fully resolve the numerical fracture issue. The reference configuration in conventional MPM is at the current time step, motivating Vaucorbeil et al. [5] to explore the total Lagrangian formulation (TLMPM), a paradigm commonly used in FEM [44]. They further extended this framework in [45] to handle solid collisions. Explicit mixed TLMPM was proposed in [46] to avoid volumetric locking in incompressible soft materials. In the graphics community, Su et al. [6] first introduced TLMPM and later extended it to A-ULMPM. However, their method still relied on a single velocity grid for unified simulation and thus exhibited sticky boundary artifacts.

3 TOTAL LAGRANGIAN MPM

To enable large deformation of solids in MPM-based fluid–solid coupling, we adopt the TLMPM from the computational mechanics community. In Sec.3.1, we provide a derivation of the internal force formulation for TLMPM based on the weak form of the momentum equation, rather than relying on the energy derivative [6]. To support more general scenarios involving contact between solids and self-contact within solids, we introduce the contact algorithm for TLMPM in Sec. 3.2.

3.1 Total Lagrangian Formulation

TLMPM is a hybrid grid/particle method for simulating continuum mechanics. As a variant of conventional MPM, TLMPM inherits the key advantages of both particles and grids: advection and spatial integration are performed on particles, while time integration is carried out on the background grid. All computations in the TLMPM framework are based on the initial configuration, which is called the Lagrangian formulation, while MPM is based on the current configuration, which is called the Eulerian formulation (sometimes also called the updated Lagrangian formulation [2]).

The deformation of a continuum is described by the deformation map: $\mathbf{x} = \phi(\mathbf{X}, t)$, which maps each material point $\mathbf{X} \in \Omega^0$ in the initial configuration to its current position $\mathbf{x} \in \Omega^t$ at time t. The velocity of a given material point $\mathbf{X}$ in total Lagrangian formulation is $\mathbf{V}(\mathbf{X}, t) = \partial\phi(\mathbf{X}, t)/\partial t$. Assuming $\phi(\cdot)$ is bijective, the Eulerian velocity field can be defined via the **push forward** operation as $\mathbf{v}(\mathbf{x}, t) = \mathbf{V}(\phi^{-1}(\mathbf{x}), t)$. Conversely, the operation to obtain the dual formula $\mathbf{V}(\mathbf{X}, t) = \mathbf{v}(\phi(\mathbf{X}), t)$ is called **pull back**. The deformation gradient is defined as: $\mathbf{F} = \partial\phi/\partial\mathbf{X}$. J is the determinant of the deformation gradient. In the Lagrangian framework, the motion of the continuum must satisfy the conservation of momentum, given by:

$$R^0 \frac{\partial \mathbf{V}}{\partial t} = \nabla^{\mathbf{X}} \cdot \mathbf{P} + R^0 \mathbf{g}, \tag{1}$$

where R^0 is density at time 0, $\mathbf{P}$ is the first Piola-Kirchoff stress, $\nabla^{\mathbf{X}} \cdot ()$ is the divergence operator in initial configuration and $\mathbf{g}$ is gravity.

By applying a test function and integrating Eq. (1) over the initial domain, we obtain a total Lagrangian time discretization of the weak form of the momentum equation. After enforcing Dirichlet boundary conditions and omitting the gravity term, the equation simplifies to:

$$\begin{aligned} &\int_{\Omega^0} R(\mathbf{X}, 0) \frac{\partial \mathbf{V}(\mathbf{X}, t)}{\partial t} \mathbf{Q}(\mathbf{X}, t) d\mathbf{X} \\ &= -\int_{\Omega^0} \mathbf{Q}_{\alpha,\beta}(\mathbf{X}, t) P_{\alpha\beta}(\mathbf{X}, t) d\mathbf{X}, \end{aligned} \tag{2}$$

where $\mathbf{Q}(\mathbf{X}, t) : \Omega^0 \to \mathbb{R}^d$ represents the test function evaluated in the initial configuration. The notation follows index conventions: $\mathbf{Q}_\alpha, V_\alpha$ are vector components, $P_{\alpha\beta}$ is a matrix entry and $\mathbf{Q}_{\alpha,\beta} = \partial \mathbf{Q}_\alpha / \partial \mathbf{X}_\beta$ is the partial derivative.

Following the similar derivation steps of MLSMPM [39], we discretize the weak form and obtain the calculation formula of the internal force $\mathbf{f}_i$ on the initial grid:

$$\mathbf{f}_i = -\sum_p V_p^0 \mathbf{P}(\mathbf{F}_p) \nabla^{\mathbf{X}} W_i(\mathbf{X}_p) \tag{3}$$

Here, W_i is the quadratic B-spline interpolation function, V_p^0 is the initial particle volume, $\nabla^{\mathbf{X}}()$ is the gradient operator in the initial configuration. This result is consistent with the internal force directly given in [5]. When energy exists, we can further replace $\mathbf{P}(\mathbf{F}_p)$ in the above formula with $\frac{\partial \Psi}{\partial \mathbf{F}}(\mathbf{F}_p^n)$, which is consistent with the force formulation

derived from the energy derivative [6]. The Hessian and the deformation gradient update of TLMPM can be seen in the supplementary material.

Unlike EMPM, TLMPM is entirely based on the initial configuration. This distinction avoids the severe cell-crossing and numerical fracture issues in MPM simulations, resulting in more stable and evenly distributed large-deformation visual animations.

3.2 Contact

Since TLMPM does not track the current grid, it inherently lacks the automatic no-slip contact handling that is naturally supported in EMPM. Additional collision processing mechanisms need to be introduced. The Lagrangian force model proposed by Jiang et al. [47] utilizes the current grid to resolve collisions, which is suitable for finite elements, spring-mass systems, etc. However, adopting such a model in TLMPM would require two grids, the initial grid and the current grid. Multiple P2G and G2P will cause tricky modal problems during collision and deformation processes, which requires further study.

We adopt the contact handling strategy proposed in de Vaucorbeil et al. [45], which determines the occurrence of a collision by directly testing for pairwise particle overlap in the current configuration, and resolves collisions by applying repulsive forces to eliminate interpenetration. Each material point p is assigned an effective radius $r_p = 1/2(V_p^0)^{1/3}$, where V_p^0 denotes the particle's initial volume. A contact is detected when $\delta := r_p + r_q - x_{pq} \geq 0$, where $x_{pq} = \|\mathbf{x}_q - \mathbf{x}_p\|$. To prevent interactions between initially neighboring particles, contact must additionally satisfy: $X_{pq} > r_{crit}$, where $X_{pq} = \|\mathbf{X}_q - \mathbf{X}_p\|$ and r_{crit} is set to $1.5(r_p + r_q)$.

The formula for the contact force is:

$$\mathbf{f}_{pq}^c = \frac{1}{\Delta t^2} \frac{m_p m_q}{m_p + m_q} \left(1 - \frac{r_p + r_q}{\|\mathbf{x}_{pq}\|}\right) \mathbf{x}_{pq}, \tag{4}$$

where m is the mass of the material point and Δt is the time step. Finally, the force is incorporated as an external force into TLMPM grid update via P2G, computed as $\mathbf{f}_i^c = \sum_p W_i(\mathbf{X}_p)\mathbf{f}_p^c$, where $\mathbf{f}_p^c = \sum_q \mathbf{f}_{pq}^c$. This method is a penalty force method without requiring additional hyper-parameter tuning. Furthermore, it resolves collisions at the particle level to capture subgrid information.

4 COUPLING

We now introduce the method of coupling TLMPM solids and Eulerian fluids. We begin by formulating the governing equations for both solid and fluid domains, incorporating pressure into the TLMPM solid model to ensure consistency with fluid interactions. We then derive the weak form of the equation and construct its corresponding linear system in space-time discretization. Finally, we introduce our new coupling scheme designed to robustly handle fluid–solid interactions under large deformations.

4.1 Governing Equation

As mentioned above, the topology of fluids changes frequently. Unless modeling special phenomena such as surface tension or vortices, the rest shape of the fluid is rarely referenced. Therefore, it is more appropriate to describe fluid behavior using quantities defined in the current configuration. The conservation of mass and momentum in the Eulerian formulation is as follows:

$$\frac{D\rho^f}{Dt} + \rho^f \nabla \cdot \mathbf{v}^f = 0, \tag{5}$$

$$\rho^f \frac{D\mathbf{v}^f}{Dt} - \nabla \cdot \sigma^f - \rho^f \mathbf{g} = 0, \tag{6}$$

where ρ is density, $\mathbf{v}$ is velocity, σ is the Cauchy stress. Mass conservation reduces to $\nabla \cdot \mathbf{v}^f = 0$ under the incompressible condition. In inviscid fluids, the stress tensor is purely isotropic with no deviatoric component, reducing to $\sigma^f = -p^f \mathbf{I}$. Thus, we further have:

$$\rho^f \frac{D\mathbf{v}^f}{Dt} + \nabla p^f - \rho^f \mathbf{g} = 0, \tag{7}$$

where p^f is the fluid pressure.

The governing equations for the solid$(\cdot)^s$ in total Lagrangian view is Eq.(1) and:

$$\frac{\partial}{\partial t}(R^s J^s) = 0. \tag{8}$$

where $J^s = \det(\mathbf{F}^s)$.

At the fluid-solid interface, the following continuity condition of normal velocity and pressure should be satisfied:

$$\left(\mathbf{v}^s - \mathbf{v}^f\right) \cdot \mathbf{n}^s = 0, \tag{9}$$

$$p^s - p^f = 0. \tag{10}$$

$\mathbf{n}^s$ is the normal direction of the solid at the interface, which is sufficient for our fluid-solid coupling task. The boundary condition here constrains only the normal velocity at the fluid–solid interface, allowing the fluid to flow freely along the tangential direction.

Note that Eq.(7) and the incompressible condition govern the Eulerian fluid in the current configuration, whereas Eq.(1) and Eq.(8) govern the solid in the initial configuration. The core coupling challenge arises because the physical continuity conditions (Eq.(9-10)) must be evaluated at the fluid-solid interface Γ in the current configuration, necessitating a consistent mapping mechanism between the two configurations.

4.2 Mixed Solids using total Lagrangian

The velocity-pressure formulation introduces pressure into the solid, increasing the solid's degrees of freedom, and is a common way to address volumetric locking in compressible solids. Introducing pressure DoFs P^s in the initial configuration improves the physical realism and stability of compressible solid simulations under large deformation, while structurally aligning the solid formulation with pressure-based incompressible fluid solvers. This alignment is crucial for constructing a monolithic, pressure-only system in our DIQ-MPM framework, ultimately enabling consistent and efficient two-way coupling between fluids and solids. We augment the solid's energy with a volume conservation term:

$$\Psi^v\left(J^s\right) = \frac{1}{2}\lambda^v\left(J^s - 1\right)^2, \tag{11}$$

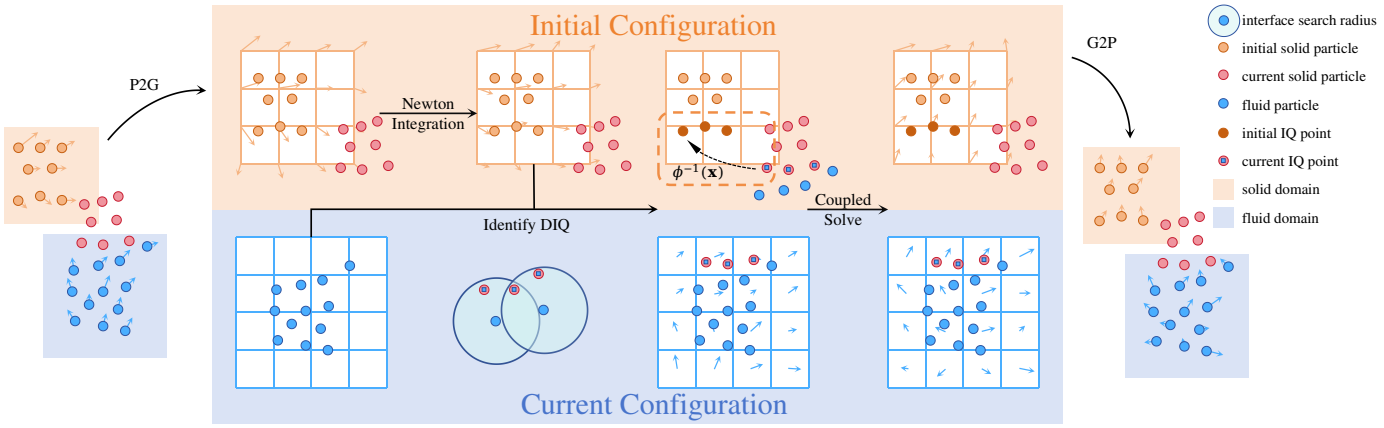

Fig. 2: **Algorithm overview.**This figure shows an overview of our algorithm. The fluid operates in the **Current Configuration** while the total Lagrangian solid is solved in the **Initial Configuration**. During coupling, fluid particles identify neighboring solid particles as current IQ points via neighbor search. Inverse deformation map $\phi^{-1}(\cdot)$ is then used to retrieve the corresponding initial IQ points, forming a dual interface(highlighted in the dashed box)

. More details about IQ point construction and the overall algorithmic overview can be found in Sec.4.6 and Sec.5.1.

where λ^v is set to half the solid Lamé's first parameter. By taking the derivative of this potential with respect to $\mathbf{F}^s$, we obtain the corresponding first Piola-Kirchhoff stress contribution from the ghost term:

$$\mathbf{P}^v = \frac{\partial \psi^g}{\partial J^s}\frac{\partial J^s}{\partial \mathbf{F}^s} = -P^s J^s \mathbf{F}^{s-T}, \tag{12}$$

where the pressure P^s is defined as :

$$P^s := -\frac{\partial \psi^g}{\partial J^s}. \tag{13}$$

It is worth noting that $P^s = -\lambda^v(J^s - 1) = -\lambda^v(R^{s,0}/R^s - 1)$ gives the EOS of this compressible solid. Compared to the mixed EMPM used in IQ-MPM, our velocity and pressure DoFs are both defined in the initial configuration, hence still inherit the properties of TLMPM, free of numerical fracture.

Now, the new energy density function has the following formulation: $\Psi(\mathbf{F}^s, J^s) = \Psi^s(\mathbf{F}^s) + \Psi^v(J^s)$. Substituting it into Eq.(1), we get

$$R^{s,0}\frac{\partial \mathbf{V}^s}{\partial t} = \nabla^{\mathbf{X}} \cdot \mathbf{P}^s - \nabla^{\mathbf{X}} \cdot (J^s \mathbf{F}^{s-T} P^s) + R^{s,0}\mathbf{g}. \tag{14}$$

This equation couples displacement and pressure together and gives the momentum equation of the compressible solid in the total Lagrangian formulation.

We further take the time derivative of both sides of the state equation (Eq.(13)), and by noting that $\partial J/\partial t = J\mathbf{F}^{-T} : \nabla^{\mathbf{X}}\mathbf{V}$ (see [48]), we obtain the pressure evolution equation:

$$\frac{\partial P^s}{\partial t} + \lambda^v J^s \mathbf{F}^{s-T} : \nabla^{\mathbf{X}}\mathbf{V}^s = 0. \tag{15}$$

Alternatively, this equation can be derived by substituting EOS into the mass conservation equation (Eq. (8)). Together, Eq.(14) and Eq.(15) form a closed system for compressible solids.

4.3 Temporal discretization

Due to the difficulty of solving the fully coupled nonlinear system, we adopt a two-step operator splitting strategy commonly used in computer graphics [1], [22] for the coupled compressible solid. First, in the elastic solve step, we compute the intermediate grid velocity ($\mathbf{V}^{s,n} \to \mathbf{V}^{s,*}$) by solving the nonlinear elastic forces using a fully implicit Newton solve. Then, a projection step incorporates the effects of pressure and updates the velocity($\mathbf{V}^{s,*} \to \mathbf{V}^{s,n+1}$). This two-step update decouples the contributions of elasticity and pressure in the overall momentum update of solids and results in a more efficient computation.

The implicit elastic solve step is similar to the standard MPM elastic update (refer to Jiang et al. [48] for more details), and the specific differences have been described in Sec.3. In the projection step, the governing equations for solid and fluid components take the following temporal discretized forms:

(1) Solid momentum equation:

$$\frac{1}{\Delta t}R^{s,0}(\mathbf{V}^{s,n+1} - \mathbf{V}^{s,*}) + \nabla^{\mathbf{X}} \cdot (J^{s,n}\mathbf{F}^{s,n-T}P^{s,n+1}) = \mathbf{0}. \tag{16}$$

(2) Solid pressure evolution:

$$\frac{1}{\lambda^v \Delta t}(P^{s,n+1} - P^{s,n}) + J^{s,n}\mathbf{F}^{s,n-T} : \nabla^{\mathbf{X}}V^{s,n+1} = 0 \tag{17}$$

(3) Fluid momentum equation:

$$\frac{1}{\Delta t}\rho^{f,n}(\mathbf{v}^{f,n+1} - \mathbf{v}^{f,n}) + \nabla p^{f,n+1} = 0 \tag{18}$$

(4) Fluid pressure evolution:

$$\nabla \cdot \mathbf{v}^{f,n+1} = 0 \tag{19}$$

Eq.(16) and Eq.(18) represent the temporal discretizations of the momentum equations(Eq.(14) and Eq.(6)), with the solid velocity undergoing an additional elastic solve step. Furthermore, Eq.(17) is the temporal discretization of Eq.(15), and Eq.(19) enforces the fluid incompressible condition. Still, the solid is in the initial configuration, whereas the fluid is in the current configuration.

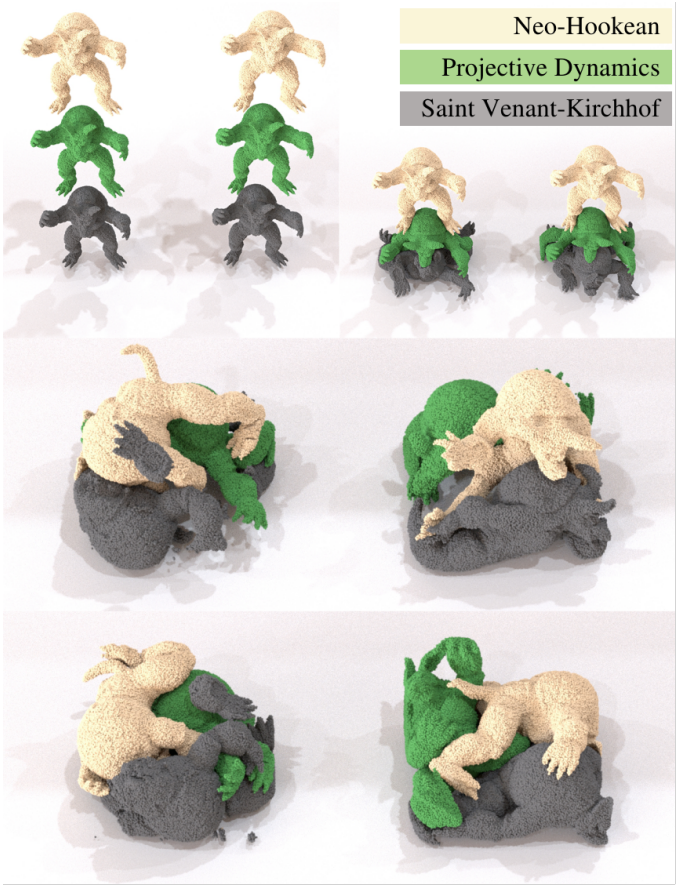

Fig. 3: **Colliding.** Armadillos with different hyperelastic models fall under gravity and collide with each other. The results on the left are generated using the mixed EMPM, while those on the right use our mixed TLMPM. The gray armadillo on the left (mixed EMPM) exhibits noticeable fracturing, while our method retains the structural integrity.

4.4 Weak Form

We solve Eqs.(16-19) using the weak form integral. After applying test functions $\mathbf{Q}^s(\mathbf{X}), T^s(\mathbf{X}), \mathbf{q}^f(\mathbf{x}), t^f(\mathbf{x})$ to both sides of the equations and integrating it w.r.t. the respective domain, we get:

$$\int_{\Omega^{s,0}} \frac{1}{\Delta t} R^{s,0}(\mathbf{V}^{s,n+1} - \mathbf{V}^{s,*}) \cdot \mathbf{Q}^s d\mathbf{X} + \int_{\Omega^{s,0}} \nabla^0 \cdot (J^{s,n}\mathbf{F}^{s,n-T}P^{s,n+1}) \cdot \mathbf{Q}^s d\mathbf{X} = \mathbf{0}, \tag{20}$$

$$\int_{\Omega^{s,0}} \frac{1}{\lambda^v \Delta t}(P^{s,n+1} - P^{s,n}) T^s d\mathbf{X} + \int_{\Omega^{s,0}} J^{s,n}\mathbf{F}^{s,n-T} : \nabla^{\mathbf{X}} V^{s,n+1} T^s d\mathbf{X} = 0, \tag{21}$$

$$\int_{\Omega^f} \frac{1}{\Delta t}\rho^{f,n}(\mathbf{v}^{f,n+1} - \mathbf{v}^{f,n}) \cdot \mathbf{q}^f d\mathbf{x} = -\int_{\Omega^f} \nabla p^{f,n+1} \cdot \mathbf{q}^f d\mathbf{x}, \tag{22}$$

$$\int_{\Omega^f} \nabla \cdot \mathbf{v}^{f,n+1} t^s d\mathbf{x} = 0. \tag{23}$$

The weak form of velocity continuity at the fluid-solid boundary Γ and the fluid domain boundary $\partial\Omega^f$ is as follows:

$$\int_{\Gamma} \left(\mathbf{v}^{s,n+1} - \mathbf{v}^{f,n+1}\right) \cdot \mathbf{n}^s \, t \, ds = 0, \tag{24}$$

$$\int_{\partial\Omega^f} \mathbf{v}^{f,n+1} \cdot \mathbf{n}^f \, t^f \, ds = \int_{\partial\Omega^f} \mathbf{v}_b \, t^f \, ds, \tag{25}$$

where $\mathbf{v}_b$ is the velocity of the slip boundary.

4.5 Spatial Discretization

To satisfy the inf-sup conditions for velocity and pressure [49], we follow the B2B0-B0-B1B0 scheme proposed by IQ-MPM [1], using quadratic B-splines to interpolate solid velocities, linear B-splines to interpolate fluid velocities, and constant B-spline curves to interpolate pressures for solids, fluids, and boundaries.

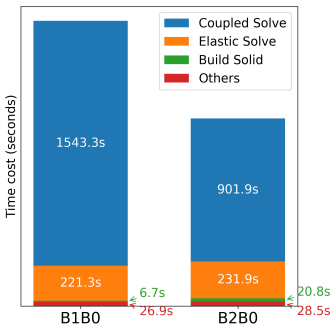

Previous work on weak form fluid–solid coupling [1], [33] suggests that using lower-order interpolation functions leads to sparser system matrices(fewer non-zero entries), thereby reducing computational cost. To mitigate the numerical fracture in MPM solids, IQ-MPM restricts the interpolation order of solid velocities to B2. The TLMPM we use completely eliminates the cell-crossing issue and numerical fracture, which allows for the use of B1 for solid velocity. However, a simple cantilever beam experiment shows that, when simulating solids using mixed TLMPM, the B2B0 model runs 1.52× faster than the B1B0 model. This can be attributed to the fact that B1 interpolation introduces discontinuities in the velocity gradient field, which worsen matrix conditioning and increase solve time, offsetting the benefit of fewer non-zero entries. As illustrated by the inset timing breakdown, although B1B0 spends less time on solid matrix assembly, it incurs a drastically higher computational cost during the coupled solve. Therefore, we still use the B2B0-B0-B1B0 scheme as an efficiency consideration.

We discretize the velocity field and its associated test function using nodal basis functions, expressed as: $\mathbf{V}^s(\mathbf{X}) = \sum_i \mathbf{V}_i^s W^{s,2}(\mathbf{X})$ and $\mathbf{Q}^s(\mathbf{X}) = \sum_i \mathbf{Q}_i^s W^{s,2}(\mathbf{X})$, where $W^{s,2}(\mathbf{X})$ denotes the quadratic B-spline interpolation basis. Similarly, we use $W^{s,0}(\mathbf{X}), w^{s,2}(x)$ and $w^{s,0}(x)$ to discretize (P,T),$(\mathbf{v},\mathbf{q})$ and (p,t) respectively.

We now derive the spatial discretized form of Eqs.(20-25):

$$\begin{pmatrix} \frac{1}{\Delta t}M^s & G^s & 0 & 0 & 0 & -H^{sT} \\ G^{sT} & -\frac{1}{\Delta t}S^s & 0 & 0 & 0 & 0 \\ 0 & 0 & \frac{1}{\Delta t}M^f & G^f & B^T & H^{fT} \\ 0 & 0 & G^{fT} & 0 & 0 & 0 \\ 0 & 0 & B & 0 & 0 & 0 \\ -H^s & 0 & H^f & 0 & 0 & 0 \end{pmatrix} \begin{pmatrix} V^{s,n+1} \\ P^{s,n+1} \\ v^{f,n+1} \\ p^{f,n+1} \\ y^{n+1} \\ h^{n+1} \end{pmatrix} = rhs, \tag{26}$$

where $\mathbf{h}$ and $\mathbf{y}$ denote the pressures at the fluid-solid interface and fluid boundary, respectively. These variables

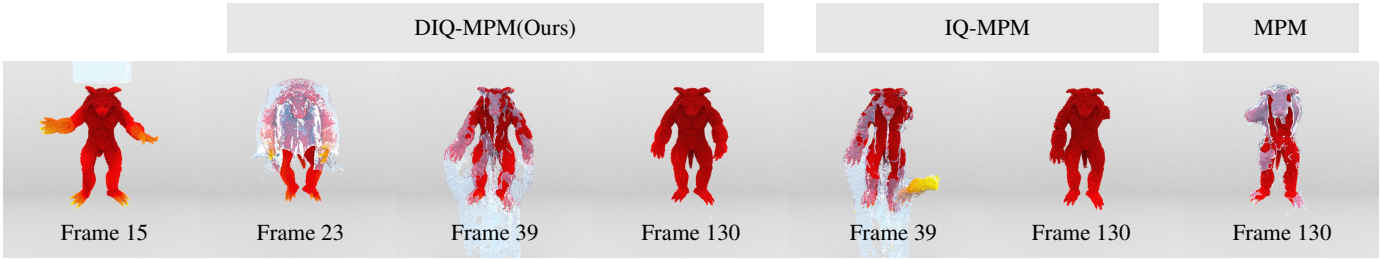

Fig. 4: **Armadillo bath.** The armadillo's head is fixed in the air while water is poured from above. The water freely slides along the solid surface. Solid particle colors indicate velocity magnitude; a linear color mapping is used from red to yellow. IQ-MPM produces visible numerical fractures. Conventional single-grid MPM not only has numerical fractures but also has fluid particles sticking to the solid surface.

can also be interpreted as Lagrange multipliers that enforce boundary conditions. The right hand side is

$$rhs = (\frac{1}{\Delta t}M^s V^{s,*}, -\frac{1}{\Delta t}S^s P^{s,n}, \frac{1}{\Delta t}M^f v^{f,n}, 0, b, 0)^T. \tag{27}$$

Here, M^s and S^s denote the lumped mass matrix and lumped stiffness matrix, respectively, obtained via the lumping technique. They take the following forms:

$$M^s_{i_\alpha i_\alpha} = \int_{\Omega^{s,0}} R^{s,0} W_i^{s,2}(\mathbf{X})\, d\mathbf{X}, S^s_{ii} = \int_{\Omega^{s,0}} \frac{1}{\lambda^v} W_i^{s,0}(\mathbf{X}) \tag{28}$$

where $\alpha = 0, 1, 2$ represents the three components of the i-th coordinate. After integrating the pressure force integration term in Eq.(20) by parts and applying the divergence theorem, we identify G^s as the discretized gradient operator in the solid domain with

$$G^s_{i_\alpha j} = -\int_{\Omega^{s,0}} J^s W_j^{s,0}(\mathbf{X}) \left(F^{-T}\nabla^{\mathbf{X}} W_i^{s,2}(\mathbf{X})\right)_\alpha d\mathbf{X}. \tag{29}$$

The lumped mass matrix, gradient, and boundary operators corresponding to the fluid domain are as follows

$$M^f_{c_\alpha c_\alpha} = \rho^f \int_{\Omega^f} w_c^{f,1}(\mathbf{x})\, d\mathbf{x}, G^f_{c_\alpha i} = -\int_{\Omega^f} w_i^{f,0}(\mathbf{x}) \left(\nabla w_c^{f,1}(\mathbf{x})\right)_\alpha d\mathbf{x},$$
$$B_{c_\alpha i} = \int_{\partial\Omega^f} w_c^{f,1}(\mathbf{x}) w_i^{f,0}(\mathbf{x}) n^f_\alpha\, ds \tag{30}$$

Zhang et al. [50] pointed out that directly computing J^s from $\mathbf{F}^s$ may introduce instabilities due to mismatched interpolation orders used in the B2B0 scheme. They suggest a separate update rule for J^s through remapping it from velocity field to pressure field. Here we use a similar remapping technique. Following Fang et al. [1], we transfer the updated pressure $P^{s,n+1}$ back to the particles in the initial configuration using $W_i^{s,0}(\mathbf{X})$, and then compute J^s via $P^s = -\lambda^v(J^s - 1)$.

4.6 Dual Interface Quadrature Coupling

The key to fluid-solid coupling is calculating the coupling term H in Eq. 26, which requires integration on the interface. In dual-grid MPM, the interface is defined on overlapping Eulerian grids [40]. However, TLMPM no longer has a current grid, preventing a consistent grid-level interface for fluid and solid. Similarly, IQ-MPM faces the same issue with staggered velocity grids. This may require the introduction

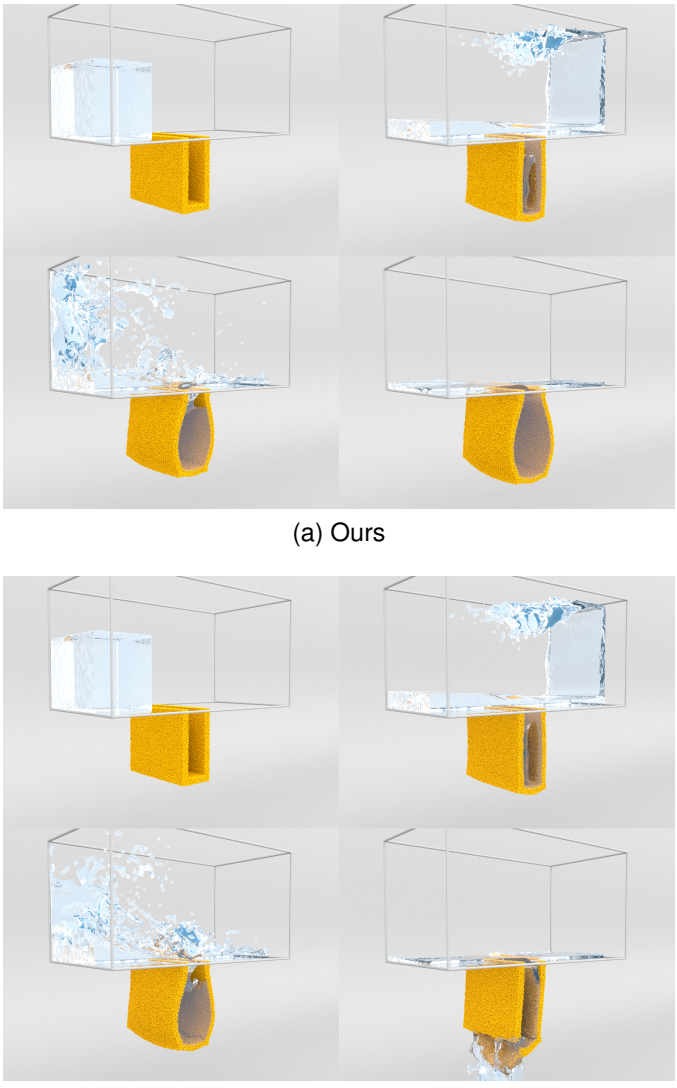

(a) Ours

(b) IQ-MPM

Fig. 5: **Bag.** A dam break scenario with an additional hole along the fluid's path, beneath which hangs an elastic bag. Our method (top) maintains fluid–solid coupling under large deformation, allowing the bag to stretch and hold the fluid without leakage. In contrast, IQ-MPM (bottom) suffers from severe numerical fracture.

of a complex cut-cell strategy for velocity interpolation. IQ-MPM solves this problem through a particle-level interface quadrature. By treating the solid particles in contact with the fluid particles as interface quadrature points and extending these points into the fluid domain, a consistent particle-level interface is obtained.

We extend this concept to coupling TLMPM solids with EMPM fluids and propose dual interface quadrature. We call the solid particles in contact with the fluid in the current configuration the current IQ points, denoted by $\mathbf{x}_q$ with a search radius of $0.5\Delta x$. Since TLMPM does not have a current grid, we cannot directly use these current IQ points now. Fortunately, TLMPM completely preserves the deformation map of the discretized material points. We can directly use $\mathbf{X} = \phi^{-1}(\mathbf{x}, t)$ to map the current IQ point back to the initial configuration and obtain the initial IQ point $\mathbf{X}_q$. Afterwards, we extend these current IQ points to the fluid domain, just like IQ-MPM does. In this way, the fluid domain can be integrated on the current interface, while the solid domain can be integrated on the corresponding initial interface. We call this dual interface quadrature.

Now, let's derive the specific form of H. Reconsider the first term of Eq.(24) and use the Lagrangian counterpart of $\mathbf{v}^s$

$$\int_\Gamma \mathbf{v}^s(\mathbf{x}, t) \cdot \mathbf{n}^s \, t(\mathbf{x}, t) \, ds = \int_\Gamma \mathbf{V}^s(\phi^{-1}(\mathbf{x}, t), t) \cdot \mathbf{n}^s \, t(\mathbf{x}, t) \, ds. \tag{31}$$

The coupling term is thus of the following pull back formula:

$$H^s_{ji_\alpha} = \int_\Gamma W_i^{s,2}(\phi^{-1}(\mathbf{x}, t)) \, w_j^{s,0}(\mathbf{x}) \, n^s_\alpha \, ds. \tag{32}$$

Our DIQ mechanism first finds the current IQ points that are close enough to the fluid particles and uses these points to discretize Eq. 32. Then the inverse of the deformation map is used to obtain the final H with

$$\begin{aligned} H^s_{ji_\alpha} &\approx \sum_q A_q \, W_i^{s,2}(\phi^{-1}(\mathbf{x}_q, t)) \, w_j^{s,0}(\mathbf{x}_q) \, n^s_\alpha \\ &= \sum_q A_q \, W_i^{s,2}(\mathbf{X}_q) \, w_j^{s,0}(\mathbf{x}_q) \, n^s_\alpha, \end{aligned} \tag{33}$$

where A_q is the cross-sectional area of the solid material point as an equivalent sphere and deformed with J^s.

Another way to think about the coupling term is to consider $\int_\Gamma \mathbf{Q}^s(\phi^{-1}(\mathbf{x}, t), t) \cdot \mathbf{n}^s \, \mathbf{h}(\mathbf{x}, t) \, ds$, where $\mathbf{h}$ is considered to be the contact force and $\mathbf{Q}^s$ distributes the force to the initial grid. Therefore, computing $H^{s^T} h$ is similar to how TLMPM computes contact forces.

The coupling term for the fluid domain is shown below

$$\begin{aligned} H^f_{jc_\alpha} &= \int_\Gamma w_c^{f,1}(\mathbf{x}) \, w_j^{f,0}(\mathbf{x}) \, n^s_\alpha \, ds \\ &\approx \sum_q A_q \, w_c^{f,1}(\mathbf{x}_q) \, w_j^{f,0}(\mathbf{x}_q) \, n^s_\alpha. \end{aligned} \tag{34}$$

4.7 Pressure Projection

The coupled system in Eq. (26) is challenging to solve directly. Fortunately, by applying a mass lumping strategy, we can obtain a sparse, Symmetric Positive Definite (SPD) system involving only the pressure-related variables (P^s, p^f, y, h) via Schur complement reduction:

$$\begin{pmatrix} A_{11} & 0 & 0 & A_{14} \\ 0 & A_{22} & A_{23} & A_{24} \\ 0 & A_{23}^T & A_{33} & A_{34} \\ A_{14}^T & A_{24}^T & A_{34}^T & A_{44} \end{pmatrix} \begin{pmatrix} P^{s,n+1} \\ p^{f,n+1} \\ y^{n+1} \\ h^{n+1} \end{pmatrix} = \begin{pmatrix} \dfrac{S^s P^{s,n}}{\Delta t} - G^{s^T} V^{s,n} \\ G^{f^T} v^{f,n} \\ B v^{f,n} - b \\ H^s V^{s,n} - H^f v^{f,n} \end{pmatrix}, \tag{35}$$

where $A_{11} = \frac{S^s}{\Delta t} + \Delta t G^{f^T} M^{s^{-1}} G^s, A_{14} = -\Delta t G^{s^T} M^{s^{-1}} H^{s^T}, A_{22} = \Delta t G^{f^T} M^{f^{-1}} G^f, A_{23} = \Delta t G^{f^T} M^{f^{-1}} B^T, A_{24} = \Delta t G^{f^T} M^{f^{-1}} H^{f^T}, A_{33} = \Delta t B M^{f^{-1}} B^T, A_{34} = \Delta t B M^{f^{-1}} H^{f^T}, A_{44} = \Delta t (H^s M^{s^{-1}} H^{s^T} + H^f M^{f^{-1}} H^{f^T})$. Finally, the computed solid and fluid pressures from Eq.(35) are substituted back into the corresponding momentum equations to recover the updated velocities $\mathbf{V}^{s,n+1}$ and $\mathbf{v}^{f,n+1}$.

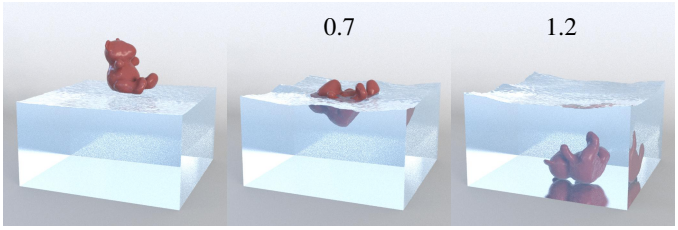

Fig. 6: **Bear.** A toy bear is dropped into still water, producing physically plausible results across different density ratios.

5 Implementation

5.1 Pipeline

We summarize our pipeline below and in Fig. 2.

(1) **Particle to grid.** Use APIC [47] to transfer the mass and velocity of solid and fluid particles to grids. The pressure of the solid is transferred to the grid through volume weighted average [1].
(2) **Solid grid update.** A fully implicit time integration is used to update the TLMPM solid velocity, where the internal force and contact force are calculated using Eq.(3) and Eq.(4), respectively.
(3) **Identify DIQ.** Current IQ points with areas and normals are identified following Sec.4.6. Current IQ points are added to the fluid domain as an interface.
(4) **Coupled solve.** Linear system Eq.(35) is constructed and solved. Calculate new velocities for solids and fluids using momentum equations.
(5) **Grid to particle.** Solid and fluid material points update their velocities and positions using APIC, respectively. Solids update their deformation gradients using $\mathbf{F}_p^{n+1} = \mathbf{F}_p^n + \Delta t \, \nabla^{\mathbf{X}} \mathbf{V}$. The solid strain J_p^s is updated following Sec.4.5.

We implement our proposed algorithm into the open source framework `ZIRAN`. SPGrid [51] is integrated to implement efficient sparse background grids to allow large-scale simulations. The fluid simulation directly follows IQ-MPM [1], using particle position clamping to improve the system condition and position correction [52] to enhance the fluid particle distribution. For solid domains, contact may also occur between the solid and the boundary. A

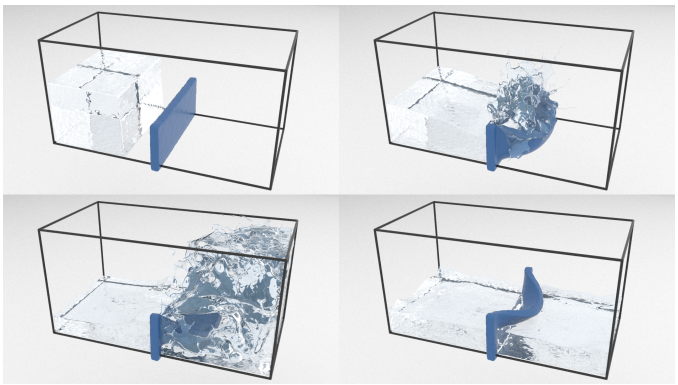

(a) Ours

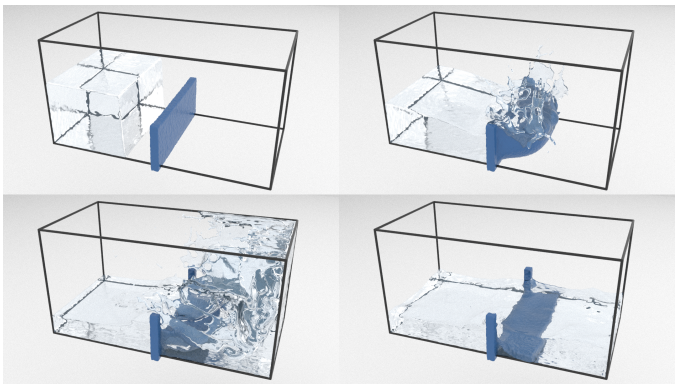

(b) IQ-MPM

Fig. 7: **Wall.** A dam break scenario with a vertical elastic wall along the fluid's path. Again, our method (top) preserves strong fluid–solid coupling and captures large wall deformations without fluid leakage. In contrast, IQ-MPM's (bottom) wall can no longer withstand the force of the fluid and breaks directly.

penalty force, similar to that used for solid contact in Sec.3.2, is applied to solid particles that penetrate the boundary in the current configuration [53]. Regarding the memory overhead, maintaining the reference configuration for the DIQ mechanism simply requires storing one additional 3D vector (the reference position $\mathbf{X}$) for each standard MPM solid particle. Therefore, the extra memory overhead is very small.

5.2 Normal Calculation

In traditional MPM, particle normals are estimated by computing and normalizing the mass gradient from the current grid. However, TLMPM does not have a current grid, making this approach inapplicable. To address this, we adopt a particle-based mass gradient formulation to calculate the normal,

$$(\nabla m^s)(\mathbf{x}_p^s) = \sum_q m_q^s \nabla N(\|\mathbf{x}_{pq}\|), \tag{36}$$

where $N(\cdot)$ is a cubic B-spline kernel with support radius $2\Delta x$. The normal is then given by $\mathbf{n}_p^s = -(\nabla m^s)(\mathbf{x}_p^s)/\|(\nabla m^s)(\mathbf{x}_p^s)\|$. This normal estimation produces stable results for coupling simulations.

5.3 Solid Contact Parameters

In this paper, the particles per cell (PPC) was set to 8 in all simulations involving TLMPM. Here, we define a uniform contact radius $0.5\Delta x$ for all particles. To further evaluate the contact algorithm, We re-run the Armadillo Bath and Colliding scenarios at a higher sampling density (PPC=16). Using the same fixed radius of $0.5\Delta x$, the simulations remained stable without any visually noticeable interpenetration.

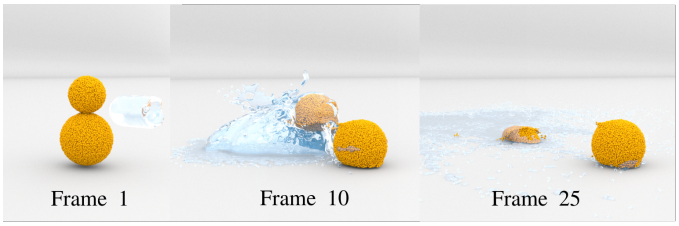

Fig. 8: **Soil.** The Granular material simulated using A-ULMPM is impacted by water.

5.4 Arbitrary Updated Lagrangian MPM

To further demonstrate the versatility of our DIQ mechanism, we extend it to a coupling scenario between EMPM fluids and solids simulated with A-ULMPM. The A-ULMPM scheme proposed by Su et al. [6] can be regarded as an intermediate formulation between TLMPM and EMPM, it adaptively updates the reference configuration, and by tuning an adaptivity parameter it can keep elastic bodies free of numerical fracture while also accommodating elasto-plastic deformations in materials such as snow and sand. This adaptivity is triggered by monitoring the local volume change J. In this subsection, we omit the superscript s for clarity in all formulas. In A-ULMPM, two deformation gradients, $\mathbf{F}^{(r,n)}$ and $\mathbf{F}^{(0,r)}$ need to be maintained, where r denotes the reference configuration. It can be seen that EMPM corresponds to choosing $r = n$, while TLMPM corresponds to $r = 0$. A-ULMPM defined $\delta J = \left|J^{(r,n)} - J^{(r,r)}\right|$, where$J^{(r,n)}$ is the determinant of $F^{(r,n)}$, and $J^{(r,r)} = 1$. Particles with $\delta J_p \geq \varepsilon$ are marked as undergoing large deformation, and the number of marked particles is denoted by n_{mp}. If $n_{\mathrm{mp}}/n_{\mathrm{p}} \geq \eta$, where n_{p} is the total number of particles, the reference configuration is updated from time step r to time step n.

The main difference in A-ULMPM is that momentum update, stress evaluation, and deformation gradient evolution are all calculated with respect to an adaptively updated reference configuration. We refer the reader to [6] for details. In Eq. (11), we defined $J = J^{0,n} = \det(\mathbf{F}^{(0,n)})$ as the volume ratio from the initial configuration to the current configuration. In the A-ULMPM setting, we update Eq. (11) by evaluating the volume penalty based on J measured from the reference configuration,

$$\Psi^v\left(J^{(r,n)}\right) = \tfrac{1}{2}\lambda^v\left(J^{(r,n)} - 1\right)^2, \tag{37}$$

the associated pressure $\widetilde{P}$ is also defined in the reference configuration, here we use superscript $\widetilde{(\cdot)}$ to denote physical quantities in the reference configuration. For the coupling term, analogous to Eq. (31), we work with the counterpart of

$\mathbf{v}^s$ defined on the reference configuration. Let $\widetilde{\mathbf{x}} = \widetilde{\phi}^{-1}(\mathbf{x}, t)$ map the current position $\mathbf{x}$ back to $\widetilde{\mathbf{x}} \in \Omega^r$. Substituting

$$\mathbf{v}^s(\mathbf{x}, t) = \widetilde{\mathbf{v}}^s\big(\widetilde{\phi}^{-1}(\mathbf{x}, t), t\big) \tag{38}$$

into Eq. (31) and then discretizing yields the corresponding coupling operator $\mathbf{H}$ in the A-ULMPM setting.

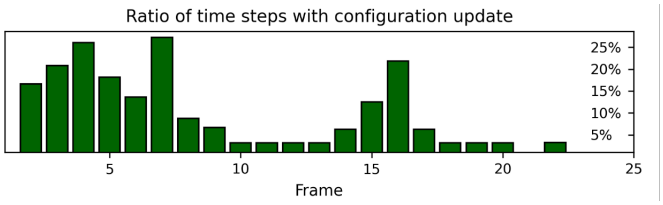

Fig. 9: Ratio of time steps requiring configuration updates over time. Two peaks around frames 5 and 15 correspond to the moments when the soil collides with the water and with the ground, respectively, during which configuration updates become more frequent.

Replacing TLMPM with A-ULMPM, the particle-level DIQ mechanism enables stable simulation of coupled scenarios involving granular-like solids. Unlike IQ-MPM, our method allows controllable updates of the solid reference configuration during the coupling process. Fig. 8 shows an example of water impacting granular material, with parameters ε and η both set to 0.01 (consistent with A-ULMPM recommendations).

6 Results

All our experiments are performed on an Intel Core i9-13900K CPU. All settings and timing are documented in Table. 1. We use OpenVDB [54] to reconstruct the fluid surface.

In most experiments, PPC for both solid and fluid materials was set to 8. In the soil experiment, the PPC for both solid and fluid materials was set to 27. Under the current Young's modulus and gravity settings, we observe severe numerical fractures in several classical scenarios when using the mixed EMPM. In contrast, our mixed TLMPM completely eliminates cell-crossing artifacts and numerical fractures, even under extreme collisions and large deformations(Fig. 3). Our method supports a variety of elasticity models, including the Projective Dynamics model, the Neo-Hookean model, and the Saint Venant–Kirchhoff model.

At the core of our method is a novel DIQ coupling mechanism, which enables MPM-based simulation of large deformation solids interacting with fluids under free-slip boundary conditions. This allows us to robustly simulate fluid–solid coupling phenomena with different density ratios, including solid collisions (Fig. 6, Fig. 10). Compared to conventional single-grid MPM and two-grid IQ-MPM methods, our approach not only enforces accurate free-slip boundary conditions but also avoids severe numerical fracture (Fig. 4). It can handle challenging large deformation scenarios (Fig. 7, Fig. 5) that many existing MPM-based fluid–solid coupling methods fail to simulate. Furthermore, we extend our method to A-ULMPM to demonstrate its scalability as a particle-level coupling mechanism(Fig. 8).

Fig. 10: **Balls.** Multiple bouncy balls with different densities experience a dam break and eventually stay calm in water.

7 Conclusion and Discussion

We propose a dual interface quadrature scheme for coupling Eulerian fluids with solids with different reference configurations. By leveraging a reversible deformation map between the reference and current configurations, we construct a particle-level dual interface that allows fluid particles to move freely along the surface of solids. This unified viewpoint makes it straightforward to switch between EMPM, TLMPM and A-ULMPM within a single framework. From an implementation standpoint, the scheme can be integrated into an existing IQ-MPM codebase with a few changes, mainly involving the solid solver in the corresponding reference configuration, as well as the newly derived gradient operator G and coupling operator H.

Although DIQ-MPM robustly handles large-deformation fluid-solid coupling, extreme deformations may still cause solid particles to become sparsely distributed, which in turn reduces the effective sampling of IQ points in the current configuration and can occasionally lead to fluid leakage into the solid. Generally, a standard PPC=8 is perfectly adequate to prevent leakage for conventional bulky solids. However, for thin-shell structures subjected to heavy fluid loads(e.g., elastic bags), severe stretching and thinning of the material exacerbate the risk of leakage. As a rule of thumb, using PPC=8 requires an initial thickness of at least $4\Delta x$; thinner shells demand a correspondingly higher PPC to prevent fluid leakage. Furthermore, since our approach successfully eliminates unwanted numerical fractures, another direction is to integrate explicit fracture models, such as the phase-field model, into our coupling framework. This would allow for the simulation of physically controllable and realistic fracture phenomena driven by strong fluid-solid interactions.

References

[1] Y. Fang, Z. Qu, M. Li, X. Zhang, Y. Zhu, M. Aanjaneya, and C. Jiang, "Iq-mpm: an interface quadrature material point method for non-sticky strongly two-way coupled nonlinear solids and fluids," *ACM Transactions on Graphics (TOG)*, vol. 39, no. 4, pp. 51–1, 2020.

TABLE 1: Time refers to the computation time per frame, measured in minutes per frame. E is Young's modulus, μ is Poisson's ratio, ρ_{solid} and ρ_{fluid} are the corresponding densities. Δt_{step} is the maximum allowed time step. The actual time step is adaptively calculated using the CFL condition to ensure that no particle moves more than $0.4\Delta x$ in one step. The densities of the balls in the Balls example are 0.5/0.7/0.9/1.1/1.3e3. The soil example adopts the granular elastoplasticity model [3] with principal stretches restricted in $(1-2.5e^{-2}, 1+7.5e^{-3})$

Example	Δt_{frame}	Δx	Δt_{step}	N_{solid}	N_{fluid}	E	μ	ρ_{solid}	ρ_{solid}	time	time$_{IQ}$
Armadillo bath	1/24	1.5/128	0.003	0.14M	0.4M	7.5e4	0.3	3e3	1e3	1.75	1.77
Bag	1/48	2/128	0.003	0.24M	0.63M	1.2e5	0.4	1.5e3	1e3	2.89	3.49
Bear	1/24	2/128	0.003	0.02M	1.04M	5e4	0.4	0.7/1.2e3	1e3	2.13/2.37	-
Wall	1/24	2/128	0.003	0.07M	0.88M	2e4	0.4	1e3	1e3	3.6	4.58
Colliding	1/48	1.5/128	0.001	0.44M	-	6e4	0.3	1e3	-	2.35	1.85
Balls	1/24	2/128	0.003	0.06M	0.78M	4e5	0.3	1e3	-	3.57	-
Soil	1/48	2/128	0.001	0.04M	0.04M	1.4e5	0.2	0.4e3	1e3	2.08	-

[2] A. De Vaucorbeil, V. P. Nguyen, S. Sinaie, and J. Y. Wu, "Material point method after 25 years: Theory, implementation, and applications," *Advances in applied mechanics*, vol. 53, pp. 185–398, 2020.

[3] A. Stomakhin, C. Schroeder, L. Chai, J. Teran, and A. Selle, "A material point method for snow simulation," *ACM Transactions on Graphics (TOG)*, vol. 32, no. 4, pp. 1–10, 2013.

[4] M. Gao, A. P. Tampubolon, C. Jiang, and E. Sifakis, "An adaptive generalized interpolation material point method for simulating elastoplastic materials," *ACM Trans. Graph.*, vol. 36, no. 6, Nov. 2017. [Online]. Available: https://doi.org/10.1145/3130800.3130879

[5] A. de Vaucorbeil, V. P. Nguyen, and C. R. Hutchinson, "A total-lagrangian material point method for solid mechanics problems involving large deformations," *Computer Methods in Applied Mechanics and Engineering*, vol. 360, p. 112783, 2020.

[6] H. Su, T. Xue, C. Han, and M. Aanjaneya, "A-ulmpm: An adaptively updated lagrangian material point method for efficient physics simulation without numerical fracture," in *Computer Graphics Forum*, vol. 41, no. 2. Wiley Online Library, 2022, pp. 325–341.

[7] D. Roble, N. b. Zafar, and H. Falt, "Cartesian grid fluid simulation with irregular boundary voxels," in *ACM SIGGRAPH 2005 Sketches*, 2005, pp. 138–es.

[8] C. Batty, F. Bertails, and R. Bridson, "A fast variational framework for accurate solid-fluid coupling," *ACM Transactions on Graphics (TOG)*, vol. 26, no. 3, pp. 100–es, 2007.

[9] Y. T. Ng, C. Min, and F. Gibou, "An efficient fluid–solid coupling algorithm for single-phase flows," *Journal of Computational Physics*, vol. 228, no. 23, pp. 8807–8829, 2009.

[10] O. Zarifi and C. Batty, "A positive-definite cut-cell method for strong two-way coupling between fluids and deformable bodies," in *Proceedings of the ACM SIGGRAPH/Eurographics Symposium on Computer Animation*, 2017, pp. 1–11.

[11] T. Takahashi and C. Batty, "Elastomonolith: A monolithic optimization-based liquid solver for contact-aware elastic-solid coupling," *ACM Transactions on Graphics (TOG)*, vol. 41, no. 6, pp. 1–19, 2022.

[12] C. Lyu, W. Li, M. Desbrun, and X. Liu, "Fast and versatile fluid-solid coupling for turbulent flow simulation," *ACM Transactions on Graphics*, vol. 40, no. 6, p. 201, 2021.

[13] D. I. Levin, J. Litven, G. L. Jones, S. Sueda, and D. K. Pai, "Eulerian solid simulation with contact," *ACM Transactions on Graphics (TOG)*, vol. 30, no. 4, pp. 1–10, 2011.

[14] Y. Fan, J. Litven, D. I. Levin, and D. K. Pai, "Eulerian-on-lagrangian simulation," *ACM Transactions on Graphics (TOG)*, vol. 32, no. 3, pp. 1–9, 2013.

[15] Y. Teng, D. I. Levin, and T. Kim, "Eulerian solid-fluid coupling," *ACM Transactions on Graphics (TOG)*, vol. 35, no. 6, pp. 1–8, 2016.

[16] A. Robinson-Mosher, T. Shinar, J. Gretarsson, J. Su, and R. Fedkiw, "Two-way coupling of fluids to rigid and deformable solids and shells," *ACM Transactions on Graphics (TOG)*, vol. 27, no. 3, pp. 1–9, 2008.

[17] J. J. Monaghan, "Smoothed particle hydrodynamics," *In: Annual review of astronomy and astrophysics. Vol. 30 (A93-25826 09-90), p. 543-574.*, vol. 30, pp. 543–574, 1992.

[18] M. Becker and M. Teschner, "Weakly compressible sph for free surface flows," in *Proceedings of the 2007 ACM SIGGRAPH/Eurographics symposium on Computer animation*, 2007, pp. 209–217.

[19] M. Ihmsen, J. Cornelis, B. Solenthaler, C. Horvath, and M. Teschner, "Implicit incompressible sph," *IEEE transactions on visualization and computer graphics*, vol. 20, no. 3, pp. 426–435, 2013.

[20] J. Bender and D. Koschier, "Divergence-free smoothed particle hydrodynamics," in *Proceedings of the 14th ACM SIGGRAPH/Eurographics symposium on computer animation*, 2015, pp. 147–155.

[21] N. Akinci, M. Ihmsen, G. Akinci, B. Solenthaler, and M. Teschner, "Versatile rigid-fluid coupling for incompressible sph," *ACM Transactions on Graphics (TOG)*, vol. 31, no. 4, pp. 1–8, 2012.

[22] A. Peer, C. Gissler, S. Band, and M. Teschner, "An implicit sph formulation for incompressible linearly elastic solids," in *Computer Graphics Forum*, vol. 37, no. 6. Wiley Online Library, 2018, pp. 135–148.

[23] T. Xie, M. Li, Y. Yang, and C. Jiang, "A contact proxy splitting method for lagrangian solid-fluid coupling," *ACM Transactions on Graphics (TOG)*, vol. 42, no. 4, pp. 1–14, 2023.

[24] M. H. Kee, K. Um, H. Kang, and J. Han, "An optimization-based sph solver for simulation of hyperelastic solids," in *Computer Graphics Forum*, vol. 42, no. 2. Wiley Online Library, 2023, pp. 225–233.

[25] J. Bonet and T.-S. Lok, "Variational and momentum preservation aspects of smooth particle hydrodynamic formulations," *Computer Methods in applied mechanics and engineering*, vol. 180, no. 1-2, pp. 97–115, 1999.

[26] D. Sulsky, S.-J. Zhou, and H. L. Schreyer, "Application of a particle-in-cell method to solid mechanics," *Computer physics communications*, vol. 87, no. 1-2, pp. 236–252, 1995.

[27] J. U. Brackbill, D. B. Kothe, and H. M. Ruppel, "Flip: a low-dissipation, particle-in-cell method for fluid flow," *Computer Physics Communications*, vol. 48, no. 1, pp. 25–38, 1988.

[28] Y. Zhu and R. Bridson, "Animating sand as a fluid," *ACM Transactions on Graphics (TOG)*, vol. 24, no. 3, pp. 965–972, 2005.

[29] G. Klár, T. Gast, A. Pradhana, C. Fu, C. Schroeder, C. Jiang, and J. Teran, "Drucker-prager elastoplasticity for sand animation," *ACM Transactions on Graphics (TOG)*, vol. 35, no. 4, pp. 1–12, 2016.

[30] M. Gao, A. Pradhana, X. Han, Q. Guo, G. Kot, E. Sifakis, and C. Jiang, "Animating fluid sediment mixture in particle-laden flows," *ACM Transactions on Graphics (TOG)*, vol. 37, no. 4, pp. 1–11, 2018.

[31] A. Stomakhin, C. Schroeder, C. Jiang, L. Chai, J. Teran, and A. Selle, "Augmented mpm for phase-change and varied materials," *ACM Transactions on Graphics (TOG)*, vol. 33, no. 4, pp. 1–11, 2014.

[32] F. Zhang, X. Zhang, K. Y. Sze, Y. Lian, and Y. Liu, "Incompressible material point method for free surface flow," *Journal of Computational Physics*, vol. 330, pp. 92–110, 2017.

[33] S. Gagniere, D. Hyde, A. Marquez-Razon, C. Jiang, Z. Ge, X. Han, Q. Guo, and J. Teran, "A hybrid lagrangian/eulerian collocated velocity advection and projection method for fluid simulation," in *Computer Graphics Forum*, vol. 39, no. 8. Wiley Online Library, 2020, pp. 1–14.

[34] A. M. Razon, Y. Chen, Y. Han, S. Gagniere, M. Tupek, and J. Teran, "A linear and angular momentum conserving hybrid particle/grid iteration for volumetric elastic contact," *Proceedings of the ACM on Computer Graphics and Interactive Techniques*, vol. 6, no. 3, 2023.

[35] X. Li, Y. Fang, M. Li, and C. Jiang, "Bfemp: Interpenetration-free mpm–fem coupling with barrier contact," *Computer Methods in Applied Mechanics and Engineering*, vol. 390, p. 114350, 2022.

[36] C. Jiang, T. Gast, and J. Teran, "Anisotropic elastoplasticity for cloth, knit and hair frictional contact," *ACM Transactions on Graphics (TOG)*, vol. 36, no. 4, pp. 1–14, 2017.

[37] X. Yan, C.-F. Li, X.-S. Chen, and S.-M. Hu, "Mpm simulation of interacting fluids and solids," in *Computer Graphics Forum*, vol. 37, no. 8. Wiley Online Library, 2018, pp. 183–193.

[38] Y. Fei, C. Batty, E. Grinspun, and C. Zheng, "A multi-scale model for simulating liquid-fabric interactions," *ACM Transactions on Graphics (TOG)*, vol. 37, no. 4, pp. 1–16, 2018.

[39] Y. Hu, Y. Fang, Z. Ge, Z. Qu, Y. Zhu, A. Pradhana, and C. Jiang, "A moving least squares material point method with displacement discontinuity and two-way rigid body coupling," *ACM Transactions on Graphics (TOG)*, vol. 37, no. 4, pp. 1–14, 2018.

[40] M. A. Homel and E. B. Herbold, "Field-gradient partitioning for fracture and frictional contact in the material point method," *International Journal for Numerical Methods in Engineering*, vol. 109, no. 7, pp. 1013–1044, 2017.

[41] L. Fan, F. M. Chitalu, and T. Komura, "Simulating brittle fracture with material points," *ACM Transactions on Graphics (TOG)*, vol. 41, no. 5, pp. 1–20, 2022.

[42] S. G. Bardenhagen, E. M. Kober *et al.*, "The generalized interpolation material point method," *Computer Modeling in Engineering and Sciences*, vol. 5, no. 6, pp. 477–496, 2004.

[43] A. Sadeghirad, R. M. Brannon, and J. Burghardt, "A convected particle domain interpolation technique to extend applicability of the material point method for problems involving massive deformations," *International Journal for numerical methods in Engineering*, vol. 86, no. 12, pp. 1435–1456, 2011.

[44] Y. Chen, Y. Han, J. Chen, S. Ma, R. Fedkiw, and J. Teran, "Primal extended position based dynamics for hyperelasticity," in *Proceedings of the 16th ACM SIGGRAPH Conference on Motion, Interaction and Games*, 2023, pp. 1–10.

[45] A. de Vaucorbeil and V. P. Nguyen, "Modelling contacts with a total lagrangian material point method," *Computer Methods in Applied Mechanics and Engineering*, vol. 373, p. 113503, 2021.

[46] Z. Zhang, Y. Pan, J. Wang, H. Zhang, Z. Chen, Y. Zheng, and H. Ye, "A total-lagrangian material point method for coupled growth and massive deformation of incompressible soft materials," *International Journal for Numerical Methods in Engineering*, vol. 122, no. 21, pp. 6180–6202, 2021.

[47] C. Jiang, C. Schroeder, A. Selle, J. Teran, and A. Stomakhin, "The affine particle-in-cell method," *ACM Transactions on Graphics (TOG)*, vol. 34, no. 4, pp. 1–10, 2015.

[48] C. Jiang, C. Schroeder, J. Teran, A. Stomakhin, and A. Selle, "The material point method for simulating continuum materials," in *Acm siggraph 2016 courses*, 2016, pp. 1–52.

[49] T. J. Hughes, *The finite element method: linear static and dynamic finite element analysis*. Courier Corporation, 2003.

[50] Z. Zhang, Z. Hu, H. Ye, H. Zhang, and Y. Zheng, "A mixed three-field total lagrangian material point method for phase-field fracture modeling of nearly incompressible rubber-like solids," *International Journal for Numerical Methods in Engineering*, vol. 124, no. 18, pp. 4097–4117, 2023.

[51] R. Setaluri, M. Aanjaneya, S. Bauer, and E. Sifakis, "Spgrid: A sparse paged grid structure applied to adaptive smoke simulation," *ACM Transactions on Graphics (TOG)*, vol. 33, no. 6, pp. 1–12, 2014.

[52] T. Kugelstadt, A. Longva, N. Thuerey, and J. Bender, "Implicit density projection for volume conserving liquids," *IEEE Transactions on Visualization and Computer Graphics*, vol. 27, no. 4, pp. 2385–2395, 2019.

[53] A. McAdams, Y. Zhu, A. Selle, M. Empey, R. Tamstorf, J. Teran, and E. Sifakis, "Efficient elasticity for character skinning with contact and collisions," in *ACM SIGGRAPH 2011 papers*, 2011, pp. 1–12.

[54] K. Museth, J. Lait, J. Johanson, J. Budsberg, R. Henderson, M. Alden, P. Cucka, D. Hill, and A. Pearce, "Openvdb: an open-source data structure and toolkit for high-resolution volumes," in *Acm siggraph 2013 courses*, 2013, pp. 1–1.

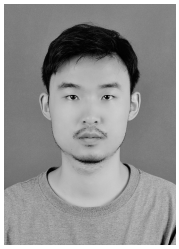

Kangrui Zhang is a PhD student at the College of Computer Science, Nankai University. He received his bachelor's degree from Northwest A&F University. His research interests include computer graphics and physically-based simulation.

Ruihong Cen is a PhD student in the School of Computing at the National University of Singapore. His research interests lie in computer graphics, specifically focusing on physically-based simulation and geometric inverse design.

Siyan Zhu received his BS and MS degrees in Computer Science from Beihang University in 2022 and 2025, respectively. His research focuses on many-body elastic simulation and accelerating physics simulation on compute-limited devices using AI and parallel computing.

Ruoyan Chen is pursuing a master's degree at the College of Computer Science, Nankai University. He received his bachelor's degree in Digital Media Technology from Jiangnan University. His research interest lies in the physically-based simulation in computer graphics.

Bo Ren received the PhD degree from Tsinghua University in 2015. He is a professor with the College of Computer Science, Nankai University. He is an associate editor of Computers & Graphics journal. His research interests involve learning-based/physically-based simulation and control, 3D neural rendering.